

Computer Vision Approach to Study Surface Deformation of Materials

Chaoyi Zhu^a, Haoren Wang^b, Kevin Kaufmann^b, Kenneth S. Vecchio^{a,b}

^aMaterials Science and Engineering Program, UC San Diego, La Jolla, CA 92093, USA

^bDepartment of NanoEngineering, UC San Diego, La Jolla, CA 92093, USA

Abstract

Characterization of the deformation of materials across different length scales has continuously attracted enormous attention from the mechanics and materials communities. In this study, the possibility of utilizing a computer vision algorithm to extract deformation information of materials has been explored, which greatly expands the use of computer vision approaches to studying mechanics of materials and potentially opens new dialogues between the two communities. The computer vision algorithm is first developed and tested on computationally deformed images (% error <0.035%), before evaluating experimentally collected images on speckle painted samples before and after deformation. Moreover, a virtual experiment has also shown the feasibility of mapping surface strain of a sample based on its natural pattern with significantly improved accuracy compared to DIC result, which provides new opportunities in experimentation and computer algorithms to study deformation mechanics of materials. Validation experiments include evaluating the performance of strain mapping using the computer vision approach in the uniaxial tensile test and three-point bending test, compared with extensometer reading and digital image correlation respectively.

1 Introduction

The state-of-the-art in extracting feature variation in images is divided into two communities: the mechanics community and the computer vision community. Although these two communities share almost the same motivations, there has rarely been any dialogue between the two [1]. The mechanics community seeks highly robust and accurate methodologies to map strains of artificial patterns painted on the objects of interest for deformation studies, whereas the computer vision community endeavors to implement a fast and simple feature- or intensity-based algorithm on an objects' natural surface pattern or texture.

In experimental mechanics, understanding how materials deform, and where they are most susceptible to failure is crucial to promote safety and potentially guide material design to alleviate catastrophic loss. Characterization methods at different length scales that can map strain in-situ and probe residual deformation post-mortem are therefore very important to provide researchers with location-specific measurable quantities to study failure mechanisms.

One of the most commonly used in-situ strain mapping techniques within the mechanics community is the digital image correlation (DIC) technique. It is a well-established non-interferometric technique, first developed by Sutton *et al.* in the 1980s, which probes the full-field surface displacement and strains in-situ with sub-pixel spatial resolution and high accuracy [2–6]. Recently, new global DIC techniques have been proposed as new alternatives to the traditional DIC [7–11]. However, the DIC or global DIC approach does not fully resolve the strain

tensor, and it is insensitive to out-of-plane or in-plane movement. A three-dimensional variant of the DIC technique is the digital volume correlation (DVC) technique based on X-ray tomography [12]. The limitation of DVC is that it relies on natural patterns found within samples to track the 3D displacement fields. It would be a difficult method for materials such as dense metal alloys that lack inherent internal patterns. Alternative diffraction-based techniques such as X-ray [13], neutron diffraction [14], or electron backscatter diffraction [15] have been established to probe the full strain (as well as rotation) tensor at microscale or even nanoscale through diffraction of a small volume of crystalline material. However, these approaches require quite complex instrumentation and analysis techniques to extract the strain data.

In the computer vision community, deformation of objects is more conveniently studied by applying the ‘demons’ algorithm on objects natural patterns. The ‘demons’ approach resembles the global DIC technique in that it also maps the non-rigid transformation of the images. More specifically, it utilizes gradient information from a fixed (deformed) image in greyscale to iteratively compute the ‘demons’ force required to ‘diffuse’ (deform) the moving (undeformed) image to match the ‘fixed’ image.

The original ‘demons’ algorithm was first developed by Thirion *et al.* as an analogy of Maxwell’s demon [16] and has later been widely implemented for many radiotherapy applications [17–21]. In the ‘demons’ registration algorithm, the displacement field, or the ‘passive’ force to register the moving image (undeformed) to the fixed image (deformed), is computed through the optical flow equation (given by Eqn. 1):

$$\vec{u} = \frac{[I_m(\vec{r}_m) - I_f(\vec{r}_f)]\nabla I_f(\vec{r}_f)}{\nabla I_f(\vec{r}_f)^2 + [I_m(\vec{r}_m) - I_f(\vec{r}_f)]^2} \quad (1)$$

where \vec{u} is the displacement field, $I_m(\vec{r}_m)$ is the intensity of point in the moving image at a position \vec{r}_m , $I_f(\vec{r}_f)$ is the intensity of point in the fixed image at a position \vec{r}_f , and $\nabla I_f(\vec{r}_f)$ is the intensity gradient of the fixed image at a position \vec{r}_f . The displacement field is calculated iteratively in the ‘demons’ algorithm followed by a Gaussian filter (variance= σ^2) to regularize the deformation field.

Registration can also be made more efficient for small deformation by considering gradient information from the moving image to allow diffusion of the fixed image into the moving image. A new ‘active’ force, proposed based on Newtons’ third law of motion, that ‘diffuses’ the fixed image to match the moving image is added by Rogelj and Lovacic [22] under the assumption of the bi-directional diffusional process. It has been shown that consistency and registration accuracy can be improved when both ‘passive’ and ‘active’ forces are treated in the same manner. Nevertheless, the ‘demons’ algorithm is still limited to measuring small deformation.

To overcome the limitation of ‘demons’ algorithm being only applicable for small deformation, a pyramidal (coarse-to-fine) multi-resolution approach is proposed by Kostelec *et al.* [23]. This approach utilizes low-resolution images derived from the original fixed and moving images to start the diffusional registration process. The displacement field derived from low-resolution images are then passed on to the next higher resolution level as a starting solution. The entire

diffusion process includes separate iterative 'demons' registration at each pyramid level, and proceeds from the lowest image resolution level to the highest image resolution level. Since the computation speed is faster for lower resolution images, the multi-resolution approach significantly improves calculation speed as well as convergence. Moreover, the *Spectral-Log Demons* algorithm has also been developed by Lombaert *et al.* to overcome the limitation of traditional 'demons' algorithms to small deformation by capturing the large deformation through Spectral Forces [24, 25]. Another interesting study dealing with large deformation by Zhao *et al.* uses a two-layer deep adaptive registration framework to separately classify the rotation parameter through convolutional neural networks and then identify scale and translation [26].

In this study, a multi-resolution image registration program is developed based on the 'demons' algorithm to resolve large deformation. The accuracy of the program is first tested in virtual deformation experiments with artificially patterned images deformed using affine transformations. From a series of parametric studies, the optimal parameters for image registration of heavily deformed images are determined based on the convergence of measured strain to expected strain in the virtual experiments. Then, the program is applied to real deformation experiments performed in the lab, including tensile deformation of pure iron (homogeneous deformation) and a three-point bending test (heterogeneous deformation). The measured axial strain in the tensile test is compared with extensometer results and the expected Green-Lagrange strain, whereas the measured heterogeneous strain in the bending test is compared with strain measured using DIC software.

2 Methodology

2.1 Implementation of 'Demons' Algorithm for Strain Mapping

In this study, the 'demons' algorithm is implemented in Matlab™; the workflow of the program is summarized in Fig. 1. The input consists of two images: one fixed image (deformed state) and one moving image (undeformed state). Before feeding the images into the 'demons' solver, a histogram matching filter and anisotropic diffusion filter are employed to balance the illumination and remove noise. Compared to a Gaussian filter, an anisotropic diffusion filter is more effective at preserving important image features such as edges, lines, etc. The two images are then down-scaled from their original resolution (at pyramid level $P_{n=0}$) according to the specified number of pyramid levels. Each added level contains a down-scaled image from the lower pyramid level by a factor of two along each coordinate direction. The image registration process begins from the highest pyramid level, i.e., lowest image resolution, and runs through an iterative process illustrated in Fig.1. The solution for the displacement field is then passed onto the lower pyramid level as an initial solution, which then significantly improves the diffusional registration. The final displacement solution is eventually generated from the lowest pyramid level containing images with the original resolution.

From the displacement field obtained through image registration in undeformed coordinates, it is then possible to obtain the Green-Lagrange strain tensor associated with it. Since direct differentiation of the displacement field in the sample coordinates is sensitive to noise, a Savitzky-Golay filter [27] is first employed to smooth the displacement field. The displacement

gradient terms are then computed locally using the central difference algorithm to obtain the corresponding deformation gradient tensor F of every point within the selected area in the undeformed coordinates. For an experiment containing larger amounts of noise, the local subset plane fitting method is implemented (given by Eqn. 2) instead of the central difference method [27].

$$F = \begin{pmatrix} 1 + \frac{\partial u_x}{\partial X} & \frac{\partial u_x}{\partial Y} \\ \frac{\partial u_y}{\partial X} & 1 + \frac{\partial u_y}{\partial Y} \end{pmatrix} \quad (2)$$

For every point in the selected area, the full 2D Green-Lagrange strain tensor, E , derived from the deformation gradient tensor, F , is then given by Equation 3, which inherently removes contribution from rigid body rotation.

$$E = \frac{1}{2}(F^T \cdot F - I) \quad (3)$$

Here, it is important to distinguish the Eulerian-Almansi strain from the Green-Lagrange strain. Since the Eulerian-Almansi strain is calculated from the deformed sample coordinates, it is therefore related to the deformation gradient tensor via a slightly different relationship:

$$A = \frac{1}{2}(I - (F \cdot F^T)^{-1}) \quad (4)$$

2.2 Virtual Experiments with Computationally Deformed Images

In this study, a series of parametric studies and validation experiments using computationally deformed images is carried out, see Fig. 2. A test image (moving image) is computationally

deformed uniaxially in tension (engineering strain in the x direction, $e_x > 0$) to obtain the deformed fixed image using an image warping method under a cubic interpolation scheme. The amount of deformation is controlled by defining the affine transformation matrix in Eq. 5.

For example, tensile deformation in the x-direction can be defined by assigning scale factors (e_x and e_y) on the diagonal terms. This test image is assumed to be taken from a hypothetical linear elastic material, which demonstrates significant elasticity, such that the applied longitudinal tensile strain can be easily related to the engineering strain e_y in the transverse contraction direction through the Poisson's ratio (taken as 0.3, for this example).

$$T = \begin{pmatrix} 1 + e_x & 0 \\ 0 & 1 + e_y \end{pmatrix} = \begin{pmatrix} 1 + e_x & 0 \\ 0 & 1 - 0.3e_x \end{pmatrix} \quad (5)$$

The expected in-plane Green-Lagrange strain tensor due to the computationally-applied tensile deformation can therefore be related to the applied affine transformation tensor:

$$E_{expected} = \frac{1}{2}(T^T T - I) = \begin{pmatrix} E_{xx} & E_{xy} \\ E_{yx} & E_{yy} \end{pmatrix} \quad (6)$$

The expected Eulerian-Almansi strain can be similarly obtained through:

$$A_{expected} = \frac{1}{2}(I - (T \cdot T^T)^{-1}) \quad (7)$$

2.3 Validation Experiments with Tensile Test and Three-Point Bending Test

Spray painting a black on white speckle pattern is done using a Paasche H series Airbrush and CREATEX airbrush paints. A uniform white layer is first painted on the polished sample before applying the random black speckle patterns. The black speckle size distribution in this study varies from 5 μm to 30 μm , which is sufficiently fine for the intended experiments.

A primary validation experiment was carried out to assess the performance of multi-resolution image registration on a uniformly deformed sample under tension. In this case, quasi-static tensile deformation of a dog-bone shaped pure iron sample, spray painted with black and white speckles, has been recorded with a Supereyes microscope camera (Model: B011) at a resolution of 1600 by 1200 pixels. An axial extensometer is used to measure the tensile strain of the recorded area of interest as strain validation data. The tensile test is manually stopped at ~ 0.15 engineering strain, before the axial strain reaches the limit of the extensometer.

Another validation experiment has been carried out to assess the performance of multi-resolution image registration on large-scale heterogeneous deformation. A pre-notched stainless steel Charpy impact bar is subject to three-point bending under quasi-static loading condition. The video of the deforming sample was recorded using a different camera setup, which consists of a NAVITAR's body tube lens mounted on an AMSCOPE's CMOS 5.1MP camera (model MU500).

3 Results and Discussion

3.1 Expected Strains for Computationally Deformed Images

A test image taken from a spray-painted sample is used for the following validation study for computationally deformed images. Based on the applied affine transformation, T , defined for computationally deformed images in tension ($e_x \in [0, 0.3]$), several expected measures of strains can be readily calculated as shown in Fig. 3. The engineering tensile strain e_x can be computed

from measuring the change in deformed image dimension relative to the undeformed image. In this study, the measured engineering tensile strain (red dashed line) is numerically equal to the applied scale factor (black solid line) in the affine transformation matrix, as shown in Fig. 3. In addition, the expected true strain value (blue dashed line) can be calculated using $e_t = \ln(e_x + 1)$, which sits below the engineering strain. Furthermore, the expected Green-Lagrange strain (green dashed line) and the expected Eulerian-Almansi strain (brown dashed line) are obtained using Eq. 6. and Eq. 7, respectively, which differ significantly from the engineering strain. For the following parametric studies, the Green-Lagrange strain is calculated using the 'demons' algorithm-based image registration code developed in this study, and compared to the expected Green-Lagrange strain for percentage error analysis.

3.2 The Effect of Pyramid Level on Image Registration

Determining the appropriate number of pyramid levels used for image registration is crucial in obtaining a reliable displacement field. In this part of the parametric study, the most deformed image ($e_x = 0.3$) and the undeformed image ($e_x = 0$) are used to study the minimum number of pyramid levels required to correctly obtain the displacement field by varying the number of pyramid level used from one to ten. Expected values for the Green-Lagrange tensor can be calculated using Eq. 6. For each of the registrations, the other necessary parameters such as number of iterations and SG-filter window size are kept constant throughout. At each pyramid level, 100 iterations are used, which is more than enough to converge to an accurate solution according to the next part of the parametric study. In addition, a SG-filter window size of 21 by 21 pixels is adopted. In all the parametric studies, the measured Green-Lagrange tensor values

are average values of the different strain components within the map. Care must be taken near the edges of the image where the gradient of displacement field becomes erroneous.

As shown in Fig. 4, the minimum number of pyramid levels required to reach an error below 0.1% is eight for all the measured components of the Green-Lagrange strain tensor. The top two rows of images in Fig. 4 represent the difference in image intensity values between the registered undeformed image and deformed image at each different pyramid level, which clearly shows improved registration when the number of pyramid levels is equal to or greater than eight. The error bar of the plots indicates the standard deviation of the measured strain components. It is observed that the error bars become unnoticeable as soon as the pyramid level reaches eight. As the number of pyramid level increases to ten, the percentage error increases slightly again without significantly increasing the error bars. This is likely because of error produced from registering the highest level (most blurred) image. Hence, the maximum number of pyramid levels is effectively limited by the original image resolution (1600 pixels by 1200 pixels in this study).

3.3 The Effect of Number of Iterations at Each Level on Image Registration

The diffusional image registration process is an iterative approach, which eventually allows the matching of the features. Since no convergence criteria is implemented in this study, the minimum number of iterations required to achieve accurate matching of the images is therefore very important to the determination of the strain tensor. In this section of the parametric study, the number of iterations is taken from 1 to 90 with an interval of 10 to match the most deformed

image ($e_x = 0.3$) and the undeformed image ($e_x = 0$). The SG-filter window size is 21 by 21 pixels, and the number of pyramid levels is eight. It has been shown in Fig. 5. that the components of measured Green-Lagrange strain tensor could be reduced to $\sim 0.1\%$ percentage error, when the number of iterations used at each pyramid level exceeds 40. The error bars also clearly show that the strain maps of the three tensor components immediately become uniform at 40 iterations. Increasing the number of iterations beyond 40 causes the percent error to slowly converge to smaller values.

3.3 The Effect of Savitzky-Golay Filter's Window Size on Image Registration

The Savitzky-Golay filter is applied to smooth the displacement field before strain calculation. It should be exercised with care for heterogenous deformation so that it does not remove details representing the deformation. In this part of the parameter study, the square SG filter's window size is varied from 3 by 3, 5 by 5, 7 by 7, 9 by 9, 13 by 13, 15 by 15, 21 by 21, 27 by 27, 35 by 35 and 41 by 41. The pyramid level is fixed at eight and the number of iterations used is 40. The most deformed image ($e_x = 0.3$) and the undeformed image ($e_x = 0$) are fed into the image registration program as input. As shown in Fig. 6, the accuracy of strain calculation clearly does not depend on the SG-filter's window size for the virtual tensile experiment in this study, whereas the precision of the strain field is slightly improved as shown by the error bars. An accuracy of less than 0.1% can be achieved with a window size of greater than 13 by 13. The percentage error of the measured strain all fall below 1% and steadily converges to 0.02% at increasing window size.

3.4 Virtual Tensile Test Experiment Part I: Artificial Pattern

A series of computationally deformed images, with spray-painted pattern, in tension are produced using an image warping algorithm with a predefined affine transformation matrix. The level of applied engineering strain on the image ranges from 0 to 0.3. Based on the previous parametric studies, the optimal parameters used for this virtual tensile experiment are determined to be: pyramid levels = 8, SG filter's window size = 21 by 21, number of iterations = 40. The image registration approach is then applied to map the Green-Lagrange strain tensor at each applied uniform strain level. The measured average strain values for the different components of the Green-Lagrange tensor are then compared with expected results calculated using Eq.6 for percentage error analysis as shown in Fig. 7. Percentage error analysis indicates that error falls below 0.035% for all applied strain levels. The highest error is measured at the smallest applied strain level, which suggests that the technique is likely prone to error at extremely small applied strain level which results in subpixel type change in the deformed image.

The percentage error associated with measuring Green-Lagrange strain tensor using image registration approach has also been assessed by imposing an additional 5° clockwise rotation to the deformed image, and compared with results obtained from Ncorr software (v1.2) developed by Blaber *et al.* [28]. Parameters used for Ncorr can be found in Appendix (Table 1). In this software, the normalized cross-correlation is used as an initial guess prior to the application of the nonlinear optimization algorithm i.e. Inverse-Compositional Gauss-Newton (IC-GN) method to calculate displacement gradients [6]. Although the Ncorr software implements a more sophisticated approach to calculate full-field displacement/strain, it is referred to as 'cross-

correlation' in the figures for brevity. It has been shown in Fig. 8 that both methods accurately extract the strain tensor from the undeformed reference frame. The error of all strain components is well below 1% except for the E_{yy} at the smallest applied strain. Overall, the Ncorr software seems to be slightly more accurate compared with image registration approach due to the advantage of IC-GN in terms of image alignment and efficient performance in image rotation experiment [29].

3.5 Virtual Tensile Test Experiment Part II: Natural Pattern

Another case study is done on a series of computationally deformed images with natural pattern e.g. grain boundary microstructure and back-scattered electrons' mass contrast using the same affine transformation matrices from 3.4. This image is taken from a well-polished metallic-intermetallic laminate (MIL) composite surface using a scanning electron microscope (SEM). Similarly, the image registration parameters used for this virtual tensile experiment on natural patterns are pyramid levels = 8, SG filter's window size = 21 by 21, number of iterations = 40. To demonstrate the advantage of using the image registration approach over DIC, the Ncorr software (v1.2) is used as a comparison. A table containing the parameters used in the DIC software can be found in the Appendix (Table 1).

As shown in Fig. 9, the schematic at the top includes several (not all) deformed images using affine transformation. The percentage errors associated with the calculated Green-Lagrange strain tensor derived from image registration and cross-correlation (Ncorr) have been plotted in three separate subplots for the three components in log scale for y-axis. It has been shown that

both methods are capable of accurately measuring the applied strain tensor, whereas the image registration clearly demonstrates significant improvement in percentage errors over the Ncorr software by an order of magnitude. This virtual experimental suggests that the application of image registration approach can more accurately measure the surface strain of samples with a properly exposed natural pattern.

3.6 Experimental Validation Part I: Tensile Deformation of Pure Iron

The method used to calculate the surface axial tensile strain is slightly modified from the previous parametric study in Section 3.4. Twenty-nine images are first extracted at an equal time interval from the video footage. The significant shift in the field of view in recording the video does not allow for accurate image registration between the first undeformed image and subsequent deformed images. Hence, image registration is conducted on pairs of neighboring images instead of using the first image as the reference image. Since the tensile deformation is stopped before the sample starts to neck, the deformation of the recorded part of the sample is uniform. The cumulative tensile strain can be calculated and compared with the extensometer result and the expected Green-Lagrange strain. The parameters used to carry out the image registration are: pyramid levels = 8, SG filter's window size = 21 by 21, number of iterations = 40. Since the deformation is uniform throughout, a local subset plane fitting method is adopted here to calculate the displacement gradient terms with a fitting window size of 5 by 5 [27].

It is shown that the image registration matches well with the extensometer result over the entire range in Fig. 10. However, the image registration only matches with the expected Green-

Lagrange strain until ~ 0.05 . The discrepancy between the measured Green-Lagrange strain from image registration and expected Green-Lagrange strain is quite significant above 0.05 strain. The reason for this discrepancy is that the sample surface is a free surface, which allows out-of-plane or in-plane movement or rotation of grains in a sample. The speckles painted on a grain with significant out-of-plane or in-plane motion will be registered to have lower than expected strains, leading to the strain being underestimated in comparison to the expected Green-Lagrange strain. Existing methods such as holographic interferometry is one possible method to extract the out-of-plane or in-plane displacements, but it is beyond the scope of this work [30].

3.7 Experimental Validation Part II: Three-Point Bending

In this experiment, a comparison of strain fields mapped using DIC and image registration on a pre-notched stainless-steel Charpy impact bar under three-point bend testing is presented. The DIC software (Ncorr v1.2) used in this part of the study is developed by Blaber *et al.* [28]. A table containing the parameters used in the DIC software can be found in the Appendix (Table 1). Similarly, the parameters used for image registration are: pyramid level = 8, SG filter's window size = 25 by 25, number of iterations = 70.

In Fig. 11, diffusional image matching through image registration shows that most of the image areas can be successfully registered except for a few edge regions. In this figure, the undeformed image is compared with the registered deformed image, since the Green-Lagrange strain in fact demands displacement gradients to be calculated in the undeformed coordinates. The

histograms showing the difference in the intensity values (residual intensity values) between registered and unregistered pairs of images, which indicate a significant proportion of the image intensities (in grayscale) match up very well. The orange histogram contains both the un-matched edge regions, as well as minor intensity mismatch within the registered 'black' region, i.e., the registered region is not entirely black.

From the registered images, the displacement field that deforms the undeformed image to match the deformed image can be extracted and plotted as a 2 by 1 vector in Fig. 12. This displacement vector can be compared with the displacement field calculated from cross-correlation method with matching scale bars in units of pixels. The area of interest selected in the two methods are slightly different, but they cover almost the same region underneath the notch. It can be seen from the displacement in the x-direction that the material surrounding the notch has been pushed away from the notch, meaning that the notch has been opened up. However, the material closer to the loading pin gets compressed towards the pin, which corresponds to the compressive strain E_{xx} at the bottom. Since the loading is applied axially at the center, opposite to the side with the notch, material underneath the notch gets pushed in the direction of the applied load (up in the image coordinates, but down in the sample coordinates). Material away from the notch also moves along to the direction of loading due to the fixed points by the side pins. This large-scale movement of material near the notch creates the large shear strain distribution E_{xy} across the thickness of the sample as shown in Fig. 13. The strain distributions for E_{xx} and E_{yy} in Fig. 13 share similar shapes because the tensile strain in the x-direction must be accompanied by a corresponding compressive strain in y to preserve the volume of material.

Based on the values of strain, the largest tensile strain, E_{xx} , is likely to result in the final failure of the Charpy bar.

The probability distributions for the different components of strains obtained from two different methods are directly compared. As shown in Fig. 13, the distributions for E_{xx} and E_{yy} are very similar to each other. The slight difference close to zero strain is likely due to the slightly larger region of interest chosen in the cross-correlation based method. Another clear discrepancy is observed in the shear strain, E_{xy} , distribution, where the cross-correlation method resolves more area in the sheared region, whereas the sheared region obtained from the image registration approach in Fig. 13 clearly contains a more discrete shear strain distribution.

3.8 Applications and Limitations

Application of multi-resolution 'demons' algorithm in mapping surface strain of homogeneously/heterogeneously deformed material using simple optics setup is proven to be feasible. With simple post-processing techniques such as histogram intensity adjustment and anisotropic diffusion filtering, it is possible to improve the image quality as well as strain mapping accuracy. Since the 'demons' algorithm is originally used in analyzing biomedical images, unsurprisingly, this method can not only work with spray-painted samples but also samples with a unique natural pattern such as e.g. grain boundary microstructure, mass contrast, etc. Therefore, it potentially allows mapping of strains of samples that are challenging to apply the artificial pattern on the e.g. thin and soft sample, wet/reactive material, mechanically fragile sample, etc. Nevertheless, further research is still required to enhance the robustness of this

approach for experiments with a significant shift in the field of view and to implement an automated method to adapt the multiple parameters used for registration to the imaging condition, as well as the amount of deformation.

4 Conclusion

It has been demonstrated in this study that the computer vision approach, i.e., multi-resolution 'demons' algorithm is effective in mapping surface strain with high accuracy on computationally deformed images painted with speckles used for DIC (% error <0.035%). A virtual experiment shows that it can also be used to map surface strain of samples based on its nature pattern, i.e. grain boundary microstructure and mass contrast, with an order of magnitude lower error in strain compared with DIC. In addition, experimental validation performed on experimentally collected video footage collected from spray-painted metallic samples deformed homogeneously (tensile test) or heterogeneously (bending test) show strain values comparable to the extensometer reading and DIC based strain maps, respectively.

Acknowledgment

We would like to acknowledge Cheng Zhang, Tyler Harrington, and Wayne Neilson for assistance in the experimental setup. C. Zhu would like to acknowledge the Dissertation Year Fellowship provided by the home department. K. Kaufmann was supported by the Department of Defense (DoD) through the National Defense Science and Engineering Graduate Fellowship (NDSEG) Program. K. Kaufmann would also like to acknowledge the support of the ARCS Foundation.

Appendix:

Table 1: Cross-correlation parameters used in Ncorr software (v1.2)

	Section 3.4	Section 3.5	Section 3.7
Image Resolution	1113*644	854*603 (undeformed)	2592*19444
Analysis Type	regular	regular	regular
RG-DIC Radius	25	25	25
Strain Radius	5	5	5
Subset Spacing	2	2	3
Diffnorm Cutoff	1e-06	1e-06	1e-06
Iteration Cutoff	50	50	50
Step Analysis	Enabled (Seed Propagation)	Enabled (Seed Propagation)	Disabled
RG-DIC Subset Truncation	Disabled	Disabled	Disabled
Strain Subset Truncation	Disabled	Disabled	Disabled

Reference

1. Wang Z, Kieu H, Nguyen H, Le M (2015) Digital image correlation in experimental mechanics and image registration in computer vision: similarities, differences and complements. *Opt Lasers Eng* 65:18–27
2. Sutton MA, Wolters WJ, Peters WH, et al (1983) Determination of displacements using an improved digital correlation method. *Image Vis Comput* 1:133–139
3. Pan B, Qian K, Xie H, Asundi A (2009) Two-dimensional digital image correlation for in-plane displacement and strain measurement: a review. *Meas Sci Technol* 20:62001
4. Sutton MA, Orteu JJ, Schreier H (2009) Image correlation for shape, motion and deformation measurements: basic concepts, theory and applications. Springer Science & Business Media
5. Sutton MA, McNeill SR, Helm JD, Chao YJ (2000) Advances in two-dimensional and three-dimensional computer vision. In: *Photomechanics*. Springer, pp 323–372
6. Pan B, Li K, Tong W (2013) Fast, Robust and Accurate Digital Image Correlation Calculation Without Redundant Computations. *Exp Mech* 53:1277–1289.
<https://doi.org/10.1007/s11340-013-9717-6>
7. Horn BKP, Schunck BG (1981) Determining optical flow. *Artif Intell* 17:185–203.
[https://doi.org/10.1016/0004-3702\(81\)90024-2](https://doi.org/10.1016/0004-3702(81)90024-2)
8. Odobez J-M, Bouthemy P (1995) Robust multiresolution estimation of parametric motion models. *J Vis Commun Image Represent* 6:348–365
9. Hild F, Roux S (2012) Comparison of Local and Global Approaches to Digital Image Correlation. *Exp Mech* 52:1503–1519. <https://doi.org/10.1007/s11340-012-9603-7>

10. Cheng P, Sutton MA, Schreier HW, McNeill SR (2002) Full-field speckle pattern image correlation with B-spline deformation function. *Exp Mech* 42:344–352
11. Roux S, Hild F, Berthaud Y (2002) Correlation image velocimetry: a spectral approach. *Appl Opt* 41:108–115
12. Bay BK, Smith TS, Fyhrie DP, Saad M (1999) Digital volume correlation: three-dimensional strain mapping using X-ray tomography. *Exp Mech* 39:217–226
13. Larson BC, El-Azab A, Yang W, et al (2007) Experimental characterization of the mesoscale dislocation density tensor. *Philos Mag* 87:1327–1347
14. Fitzpatrick ME, Lodini A (2003) Analysis of residual stress by diffraction using neutron and synchrotron radiation. CRC Press
15. Wilkinson AJ, Meaden G, Dingley DJ (2006) High-resolution elastic strain measurement from electron backscatter diffraction patterns: New levels of sensitivity. *Ultramicroscopy* 106:307–313. <https://doi.org/10.1016/j.ultramic.2005.10.001>
16. Thirion JP (1998) Image matching as a diffusion process: An analogy with Maxwell's demons. *Med Image Anal* 2:243–260. [https://doi.org/10.1016/S1361-8415\(98\)80022-4](https://doi.org/10.1016/S1361-8415(98)80022-4)
17. Cachier P, Pennec X, Ayache N (1999) Fast non rigid matching by gradient descent: Study and improvements of the “demons” algorithm. Tech Rep 1–25. <https://doi.org/10.1.1.35.5020>
18. Wang H, Dong L, O'Daniel J, et al (2005) Validation of an accelerated “demons” algorithm for deformable image registration in radiation therapy. *Phys Med Biol* 50:2887–2905. <https://doi.org/10.1088/0031-9155/50/12/011>
19. Guimond A, Roche A, Ayache N, Meunier J (2001) Three-dimensional multimodal brain

- warping using the demons algorithm and adaptive intensity corrections. *IEEE Trans Med Imaging* 20:58–69. <https://doi.org/10.1109/42.906425>
20. Vercauteren T, Pennec X, Perchant A, Ayache N (2009) Diffeomorphic demons: efficient non-parametric image registration. *Neuroimage* 45:S61–S72. <https://doi.org/10.1016/j.neuroimage.2008.10.040>
 21. Christen D, Levchuk A, Schori S, et al (2012) Deformable image registration and 3D strain mapping for the quantitative assessment of cortical bone microdamage. *J Mech Behav Biomed Mater* 8:184–193. <https://doi.org/10.1016/j.jmbbm.2011.12.009>
 22. Rogelj P, Kovačič S (2006) Symmetric image registration. *Med Image Anal* 10:484–493. <https://doi.org/10.1016/j.media.2005.03.003>
 23. Kostelec PJ, Weaver JB, Healy DM (1998) Multiresolution elastic image registration. *Med Phys* 25:1593–1604. <https://doi.org/10.1118/1.598403>
 24. Lombaert H, Grady L, Pennec X, et al (2014) Spectral log-demons: diffeomorphic image registration with very large deformations. *Int J Comput Vis* 107:254–271
 25. Lombaert H, Grady L, Pennec X, et al (2012) Spectral Demons—image registration via global spectral correspondence. In: *European Conference on Computer Vision*. Springer, pp 30–44
 26. Zhao L, Jia K (2015) Deep adaptive log-demons: Diffeomorphic image registration with very large deformations. *Comput Math Methods Med*. <https://doi.org/10.1155/2015/836202>
 27. Pan B (2007) Full-field strain measurement using a two-dimensional Savitzky-Golay digital differentiator in digital image correlation. *Opt Eng* 46:033601.

<https://doi.org/10.1117/1.2714926>

28. Blaber J, Adair B, Antoniou A (2015) Ncorr: Open-Source 2D Digital Image Correlation Matlab Software. *Exp Mech* 55:1105–1122. <https://doi.org/10.1007/s11340-015-0009-1>
29. Passieux J, Bouclier R (2019) Classic and inverse compositional Gauss-Newton in Global DIC. *Int J Numer Methods Eng*
30. Basehore ML, Post D (1981) Moiré method for in-plane and out-of-plane displacement measurements. *Exp Mech* 21:321–328

Figure captions:

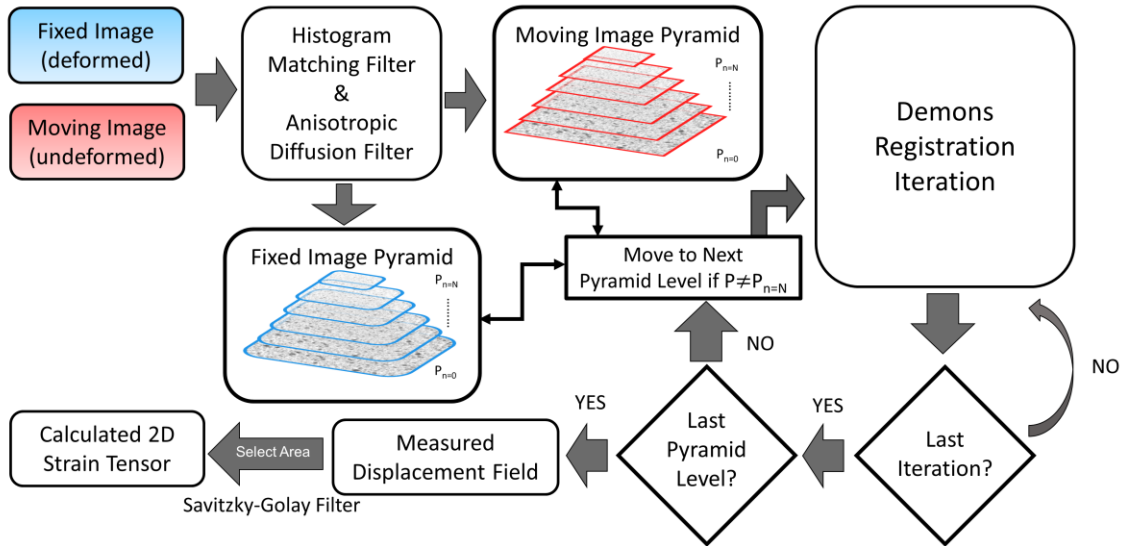


Fig.1: Flowchart of the multi-resolution image registration software developed based on the 'demons' algorithm.

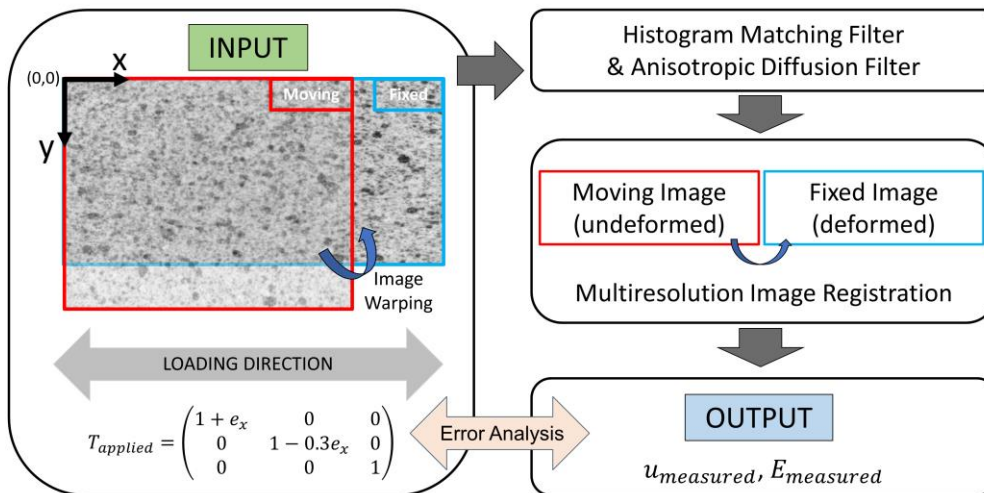


Fig.2: Flowchart of virtual deformation experiments with affine transformation and the validation of measured Green-Lagrange strain tensor with applied strain tensor.

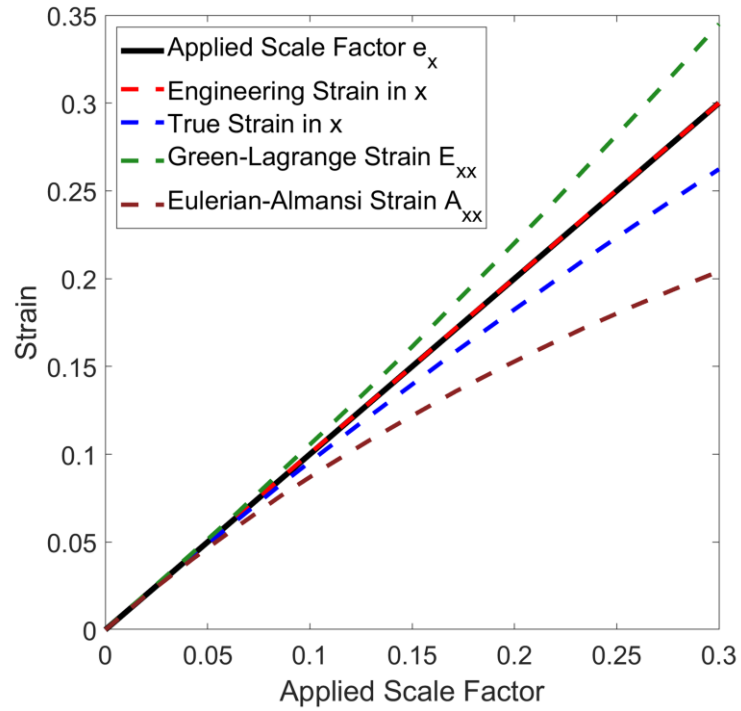


Fig.3: Different types of expected strain measures under the applied scale factor in affine transformation: engineering strain (red), true strain (blue), Eulerian-Almansi strain (brown) and Green-Lagrange strain (green).

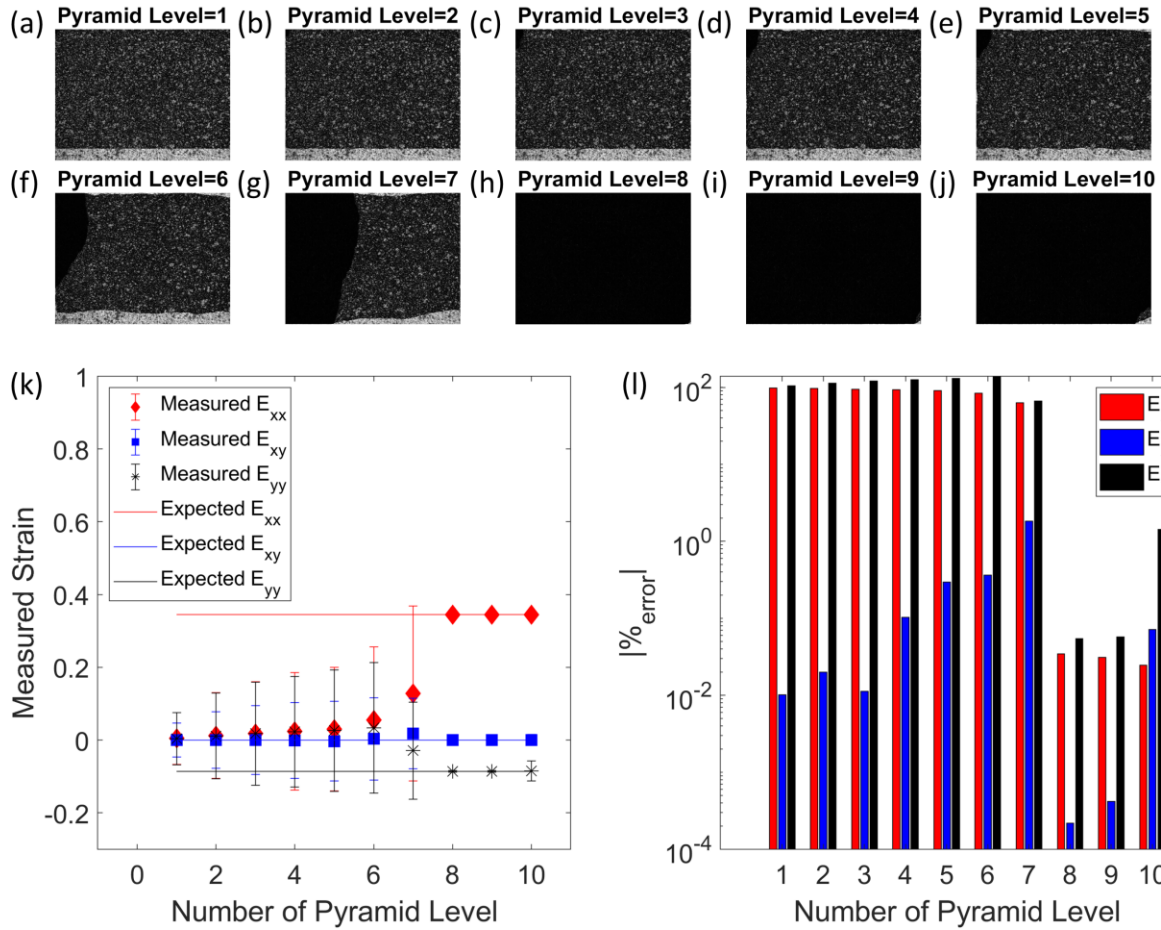


Fig.4: (a-j) Effect of using different number of pyramid levels on accuracy of image registration.

Top two rows represent the intensity difference of undeformed image and registered deformed image at different number of pyramid levels, (k) the measured average Green-Lagrange strain tensor components plotted against the expected strain tensor values as a function of number of pyramid levels, and (l) the percentage error between the measured strain tensor components and expected strain tensor components as a function of number of pyramid levels. (SG-filter window size is 21 by 21 pixels, number of iterations at each pyramid level is 100).

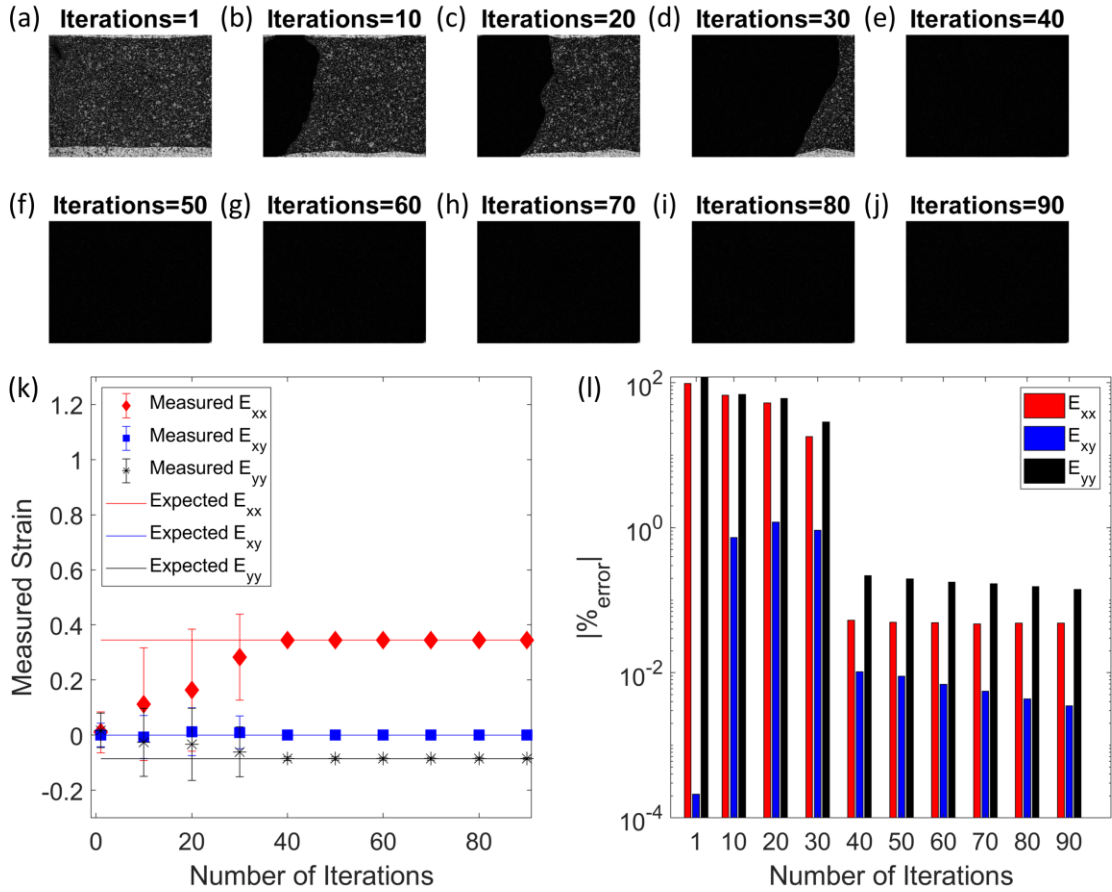


Fig.5: (a-j) Effect of using different number of iterations at each pyramid level on accuracy of image registration, (k) the measured average Green-Lagrange strain tensor components plotted against the expected strain tensor values as a function of number of iterations at each pyramid level, and (l) the percentage error between the measured strain tensor components and expected strain tensor components as a function of number of iterations for a given pyramid level. (SG-filter window size is 21 by 21 pixels, number of pyramid levels is eight).

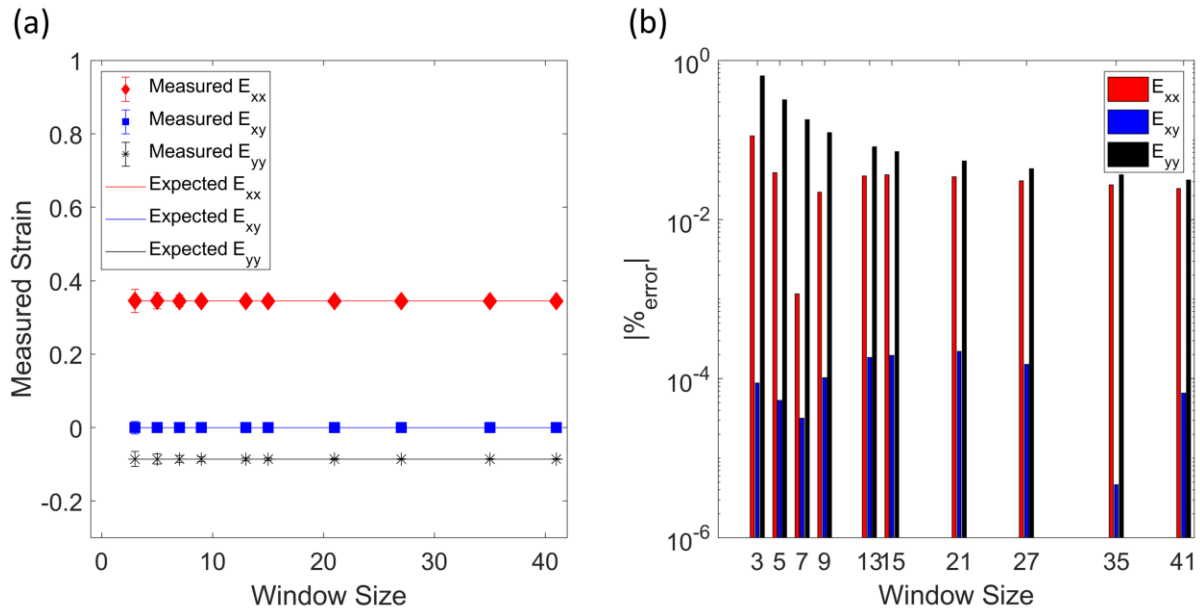


Fig.6: Effect of using different sizes of Savitzky-Golay filter windows on accuracy of image registration, (a) the measured average Green-Lagrange strain tensor components plotted against the expected strain tensor values as a function of SG filter window size, and (b) the percentage error between the measured strain tensor components and expected strain tensor components as a function of SG filter window size. (number of iterations at each pyramid level is 40, number of pyramid level is eight).

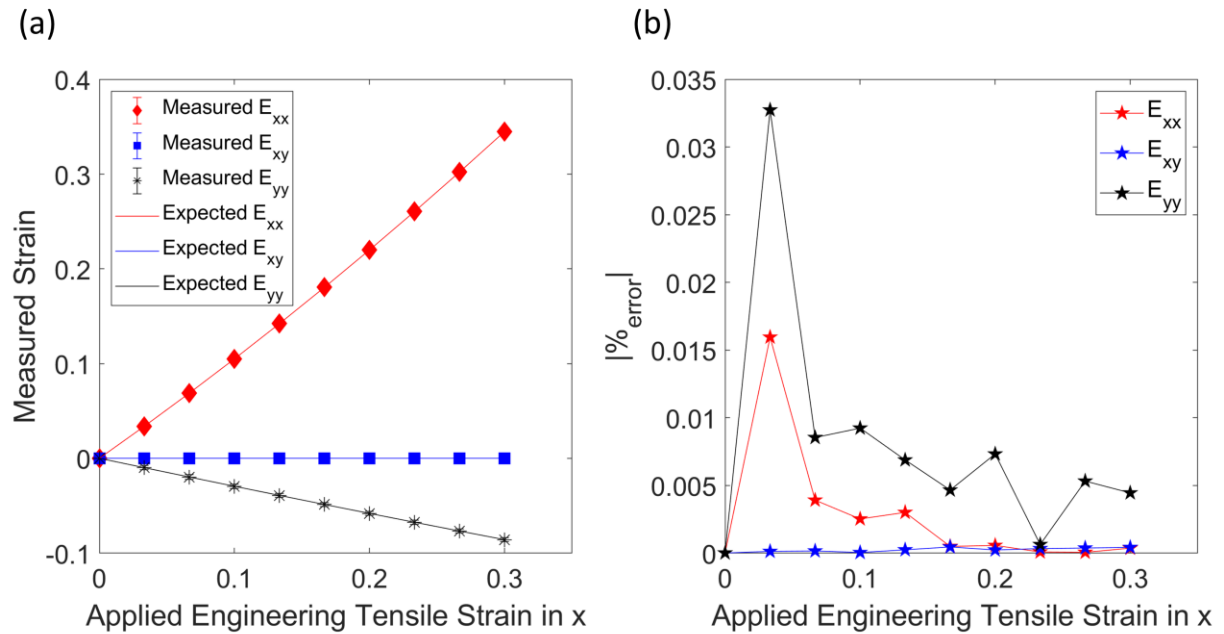


Fig.7: (a) the measured average Green-Lagrange strain tensor components plotted against the expected strain tensor values as a function of applied engineering tensile strain in the x-direction, and (b) the percentage error between the measured strain tensor components and expected strain tensor components as a function of applied engineering tensile strain in x. (number of iterations at each pyramid level is 40, number of pyramid levels is eight, SG-filter window size is 21 by 21 pixels).

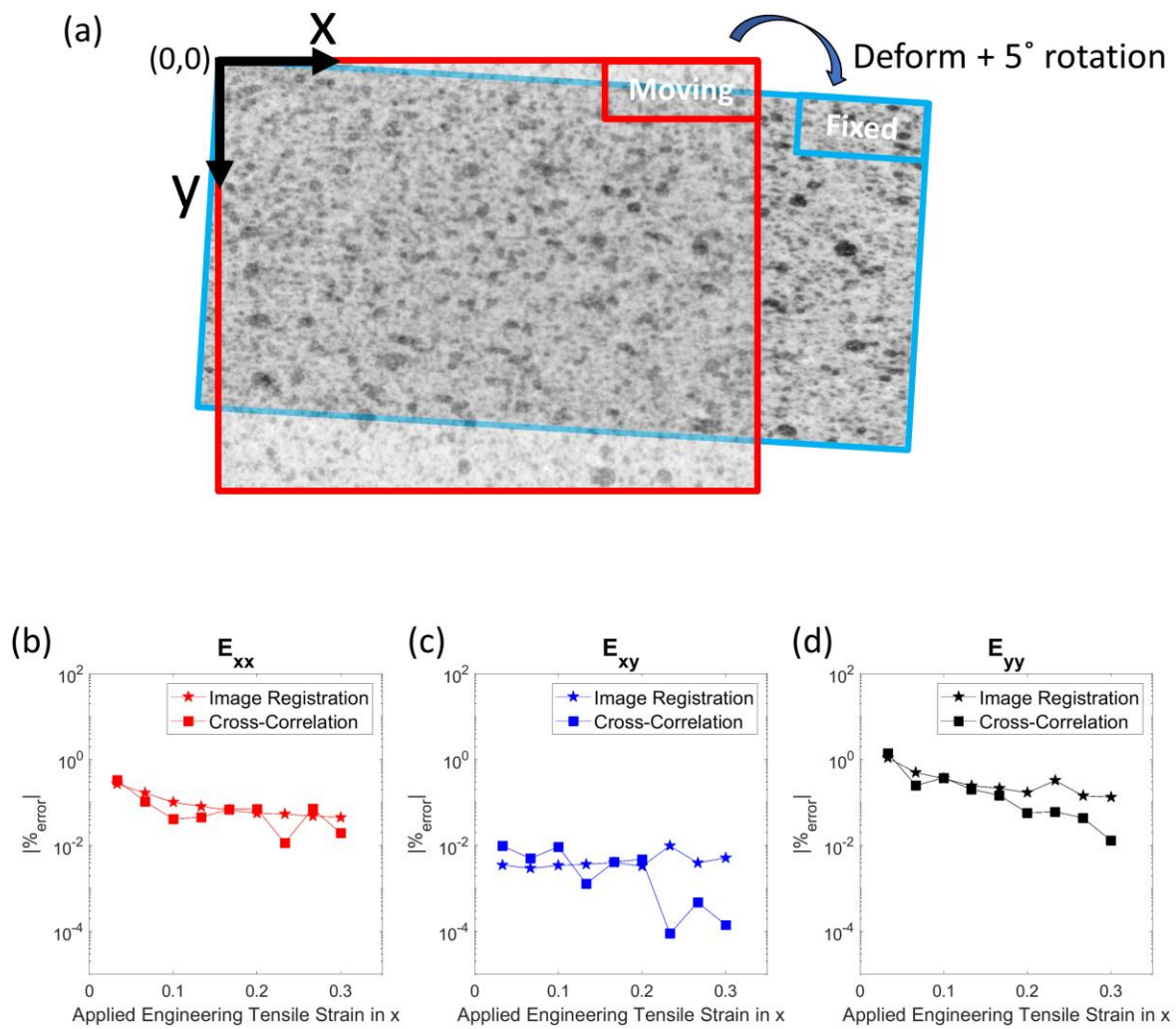


Fig.8: (a) schematic of the affine transformation (stretch) of spray-painted images plus a 5° rotation; (b-d) percentage errors of average Green-Lagrange strain tensor components E_{xx} , E_{xy} , and E_{yy} obtained from image registration and cross-correlation (Ncorr) methods.

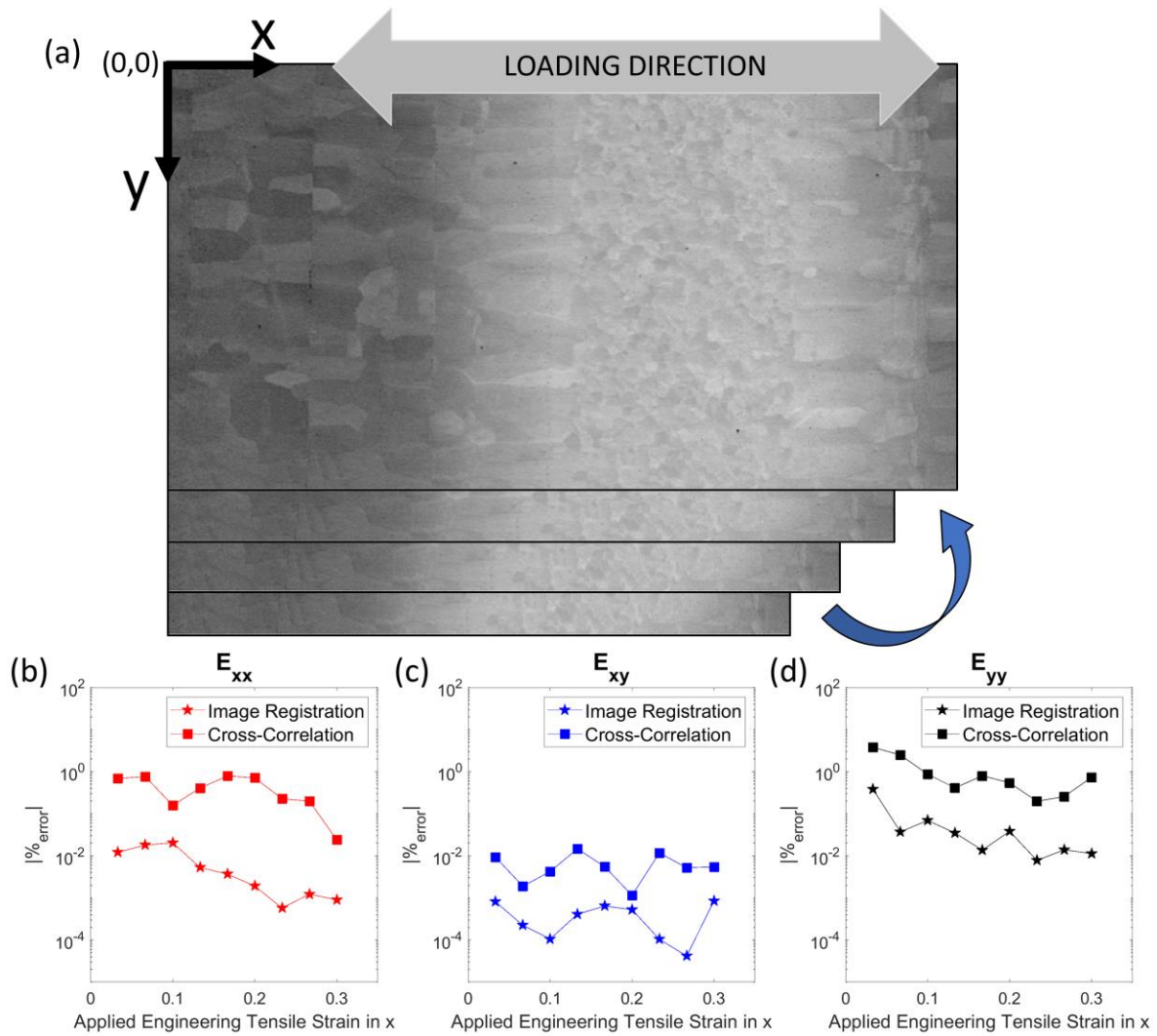


Fig.9: (a) schematic of the affine transformation (stretch) of an SEM taken from a metallic-intermetallic laminate component sample; (b-d) percentage errors of average Green-Lagrange strain tensor components E_{xx} , E_{xy} , and E_{yy} obtained from image registration and cross-correlation (Ncorr) methods.

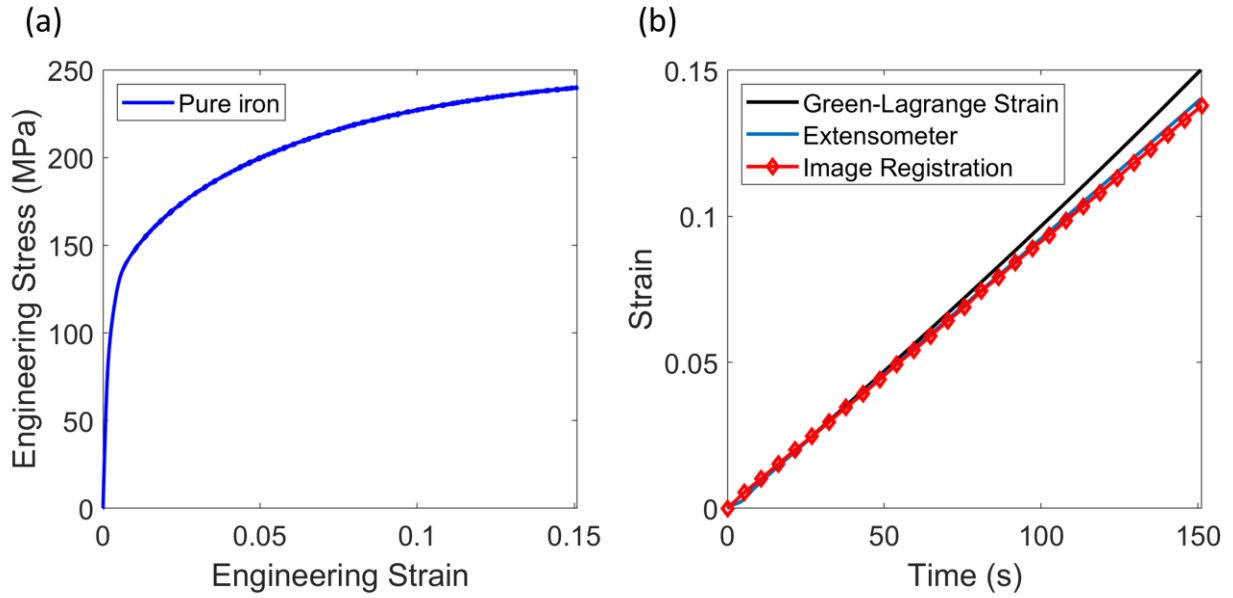


Fig.10: (a) the engineering stress-strain curve directly obtained from load frame, and (b) comparison between measured strain from both extensometer and image registration approach along with the expected Green-Lagrange axial strain.

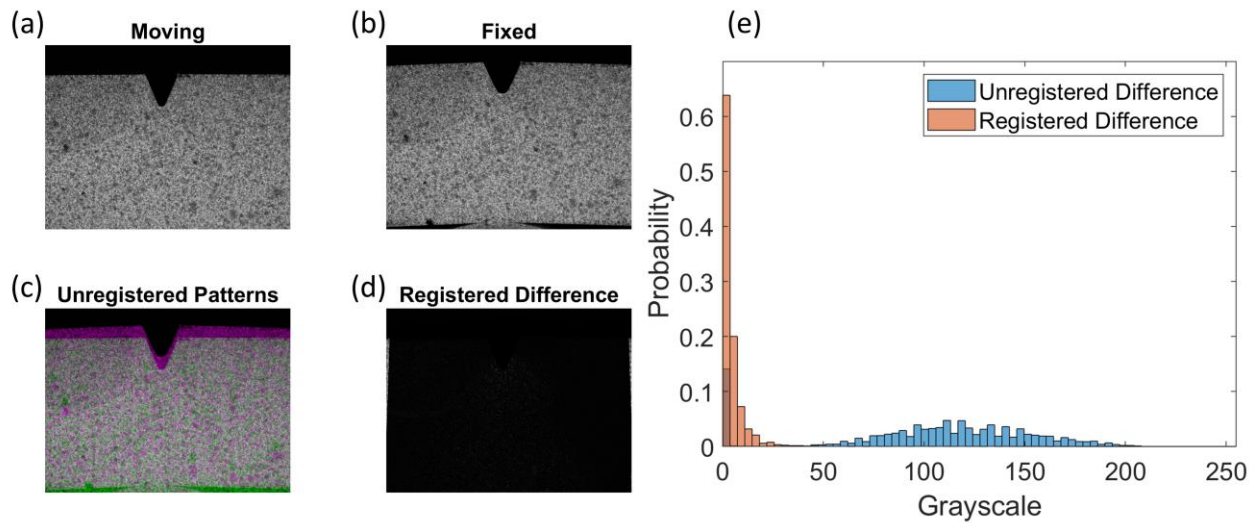


Fig.11: (a-d) the image intensity differences between unregistered deformed (fixed) and undeformed (moving) images as well as registered deformed image and undeformed

image, and (e) histograms of intensity differences of the unregistered pair of images and registered pair of images.

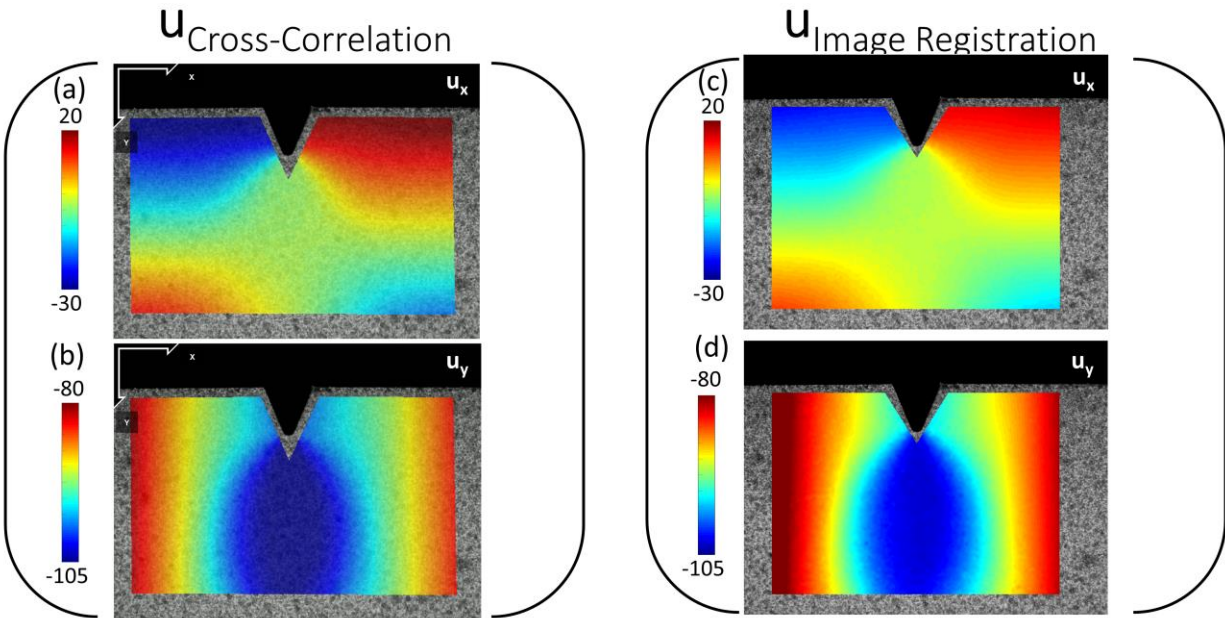


Fig.12: Displacement fields mapped using (a-b) cross-correlation-based DIC (Ncorr) and (c-d) multi-resolution image registration in a three-point bending test.

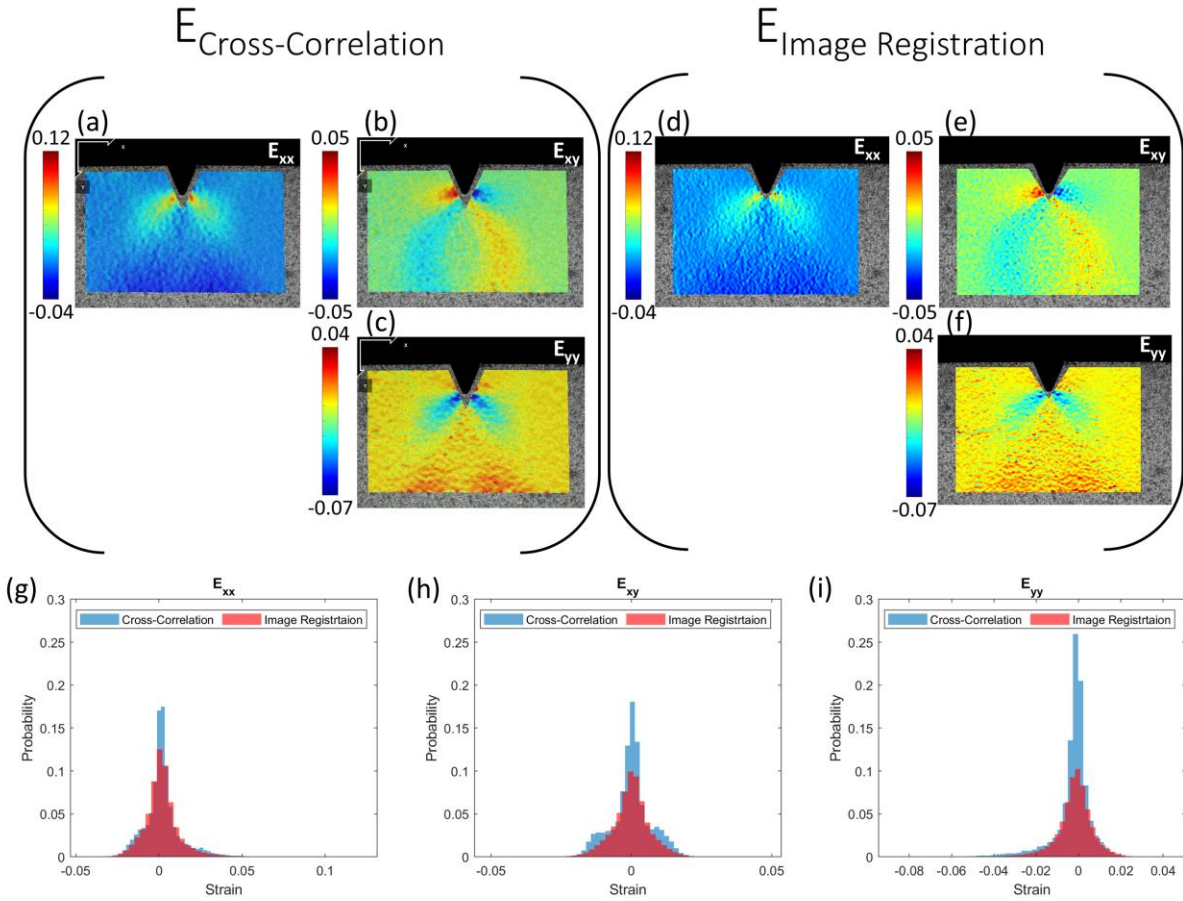


Fig.13: Green-Lagrange strain fields mapped using (a-c) cross-correlation based DIC (Ncorr) and (d-f) multi-resolution image registration in a three-point bending test, and (g-i) the comparison of histograms of strain fields mapped using cross-correlation based DIC (Ncorr) and multi-resolution image registration in a three-point bending test.